AMR for low Mach number reacting flow

John Bell

Lawrence Berkeley National Laboratory
Berkeley, CA 94720
`jbbell@lbl.gov`

Abstract

We present a summary of recent progress on the development and application of adaptive mesh refinement algorithms for low Mach number reacting flows. Our approach uses a form of the low Mach number equations based on a general equation of state that discretely conserves both mass and energy. The discretization methodology is based on a robust projection formulation that accommodates large density contrasts. The algorithm supports modeling of multicomponent systems and incorporates an operator-split treatment of stiff reaction terms. The basic computational approach is embedded in an adaptive projection framework that uses structured hierarchical grids with subcycling in time that preserves the discrete conservation properties of the underlying single-grid algorithm. We present numerical examples illustrating the application of the methodology to turbulent premixed combustion and nuclear flames in type Ia supernovae.

1 Introduction

Detailed modeling of time-dependent reacting flows with realistic reaction mechanisms places severe demands on computational resources. These computational costs can be dramatically reduced by combining a low Mach number formulation that allows a large increase in time step size with local adaptive mesh refinement to reduce the total number of computational zones that must be advanced for a specific problem. Low Mach number models analytically eliminate acoustic waves from the system while preserving compressibility effects arising from the reaction process and associated thermal behavior of the fluid. These types of models for reacting flows were first introduced by Rehm and Baum [29]. A systematic approach for deriving these types of models using aympotitics in Mach number was given by Majda and Sethian [23]. Low Mach number models replace the compressible Navier Stokes equations with

a system evolving subject to a constraint on the velocity field. Since acoustic waves have been analytically removed from the system, the time step is determined by the advective time scale of the flow.

Local refinement for steady combustion has been discussed by a number of authors. See for example, Smooke *et al.* [34], Coelho and Pereira [13], de Lange and de Goey [16], Mallens *et al.* [24] Somers and de Goey [31], Bennett and Smooke [10], Bennett *et al.* [9], Becker *et al.* [3] and the references cited in these works.

For time-dependent flows, Najm *et al.* [26] couple a local refinement algorithm for species and temperature with a vortex method for momentum. Pember *et al.* [28] present an adaptive projection algorithm for time-dependent low Mach number combustion using simplified kinetics and an assumption of unity Lewis number. The methodology in Pember *et al.* [28] uses a hierarchical structured refinement approach based on the local adaptive projection methodology developed by Almgren *et al.* [2]. The method discussed here represents a generalization of the Pember *et al.* methodology. In particular, it incorporates complex chemistry and the effects of differential diffusion as discussed in Day and Bell [15] and the extension of the methodology to non-ideal equations of state as discussed in Bell *et al.* [5]. The reader is referred to those papers for additional detail about the methodology.

We note that our basic discretization approach differs from the standard approach to solving the low Mach number system originally proposed by McMurtry *et al.* [25]. In the McMurtry *et al.* approach an auxiliary equation for the density in convective form is derived by differentiating the equation of state in time and replacing temporal derivatives of temperature and species by spatial derivatives of these quantities. This equation is then used to advance the density in time with temperature being determined from the equation of state. In the projection step, the McMurtry *et al.* algorithm solves a constant coefficient Poisson equation to modify the velocity field so that the conservation of mass equation is satisfied.

In contrast to this approach, we directly solve the conservation form of the equations for both enthalpy and density. Our projection step solves a variable coefficient elliptic equation to enforce the velocity constraint given in equations orginally introduced by Bell and Marcus [8]. This approach was first extended to combustion by Lai [21] and Lai *et al.* [22]. Related implementations or extensions include Hilditch and Colella [19] and Pember *et al.* [27]. Unlike the standard approach, the approach discussed here conserves both mass and energy; however, the evolution does not remain on the constraint imposed by the equation of state. Instead, the evolution is allowed to drift within a small neighborhood of that constraint.

In section 2, we introduce the low Mach number equations for a general equation of state. In section 3, we describe a second-order projection algorithm for integrating the low Mach number equations and give an overview of our adaptive methodology. In the final two sections we present prototype applications of this methodology to premixed turbulent combustion and nu-

clear flames. The results shown here are taken from studies presented in [7] and [6], respectively.

2 Low Mach number model

The low Mach number model is derived from the compressible flow equations using asymptotic analysis. These equations describe conservation of mass, momentum and energy augmented with equations for the species representing the composition of the fluid.

$$\frac{\partial \rho}{\partial t} + \nabla \cdot \rho U = 0$$

$$\frac{\partial \rho U}{\partial t} + \nabla \cdot (\rho U U + p) = \nabla \cdot \tau + \rho \mathbf{g}$$

$$\frac{\partial \rho E}{\partial t} + \nabla \cdot (\rho U E + p U) = -\nabla \cdot q + \nabla \cdot \tau U + \rho U \cdot \mathbf{g}$$

$$\frac{\partial \rho Y_k}{\partial t} + \nabla \cdot \rho U Y_k = \nabla \cdot \rho D_k \nabla Y_k + \rho \dot{\omega}_k$$

Here, ρ, U, T and p are the density, velocity, temperature, and pressure, respectively, and $E = e + U \cdot U/2$ is the total energy with e representing the internal energy. Note that e includes the energy of formation and mixing so that there is no explicit term in the energy equation due to reaction; those effects are implicitly included in the definition of e. (See, for example, Bird, Steward and Lightfoot [11].) In addition, Y_k is the mass fraction of species k, with associated production rate $\dot{\omega}_k$. Here, both the $\dot{\omega}_k$ and the $\rho D_k \nabla Y_k$ must sum to zero, expressing the notion that reactions conserve mass and species diffusion cannot transport net mass. For simplicity we assume a mixture model for species diffusion and ignore thermal diffusion (Soret) and Dufour effects as well as radiative heat transfer. (Generalizing the formulation to include these effects is straightforward.) For this case, the heat flux, q, is given by [1]

$$q = -\kappa \nabla T - \rho \xi_k D_k \nabla Y_k$$

with $\xi_k = \left. \frac{\partial h}{\partial Y_k} \right|_{p,T,Y_{j,j \neq k}}$, where the enthalpy, $h = e + p/\rho$. Finally, τ is the stress tensor, $\mathbf{g}$ is the gravitational force and κ is the thermal conductivity.

As a prelude to developing the low Mach number equations, we first rewrite the energy equation in terms of the enthalpy,

$$\rho \frac{Dh}{Dt} - \frac{Dp}{Dt} = \nabla \cdot \kappa \nabla T + \nabla \cdot \rho \xi_k D_k \nabla Y_k$$

---

[1]Unless otherwise noted, we use the summation convention throughout the paper.

For the low Mach number asymptotic analysis (following Majda and Sethian [23]), we introduce scaled coordinates in which the time scale is proportional to the spatial scale divided by the advective velocity scale. In this scaling, we expand pressure and velocity in Mach number, $M = U/c_s$, (c_s is the sound speed). Substituting these expansions in M into the equations of motion given above, retaining highest order terms in M we find that the $O(1)$ pressure term is independent of the spatial coordinate and the $O(M)$ pressure term is zero. Thus, in the low Mach number expansion, presure is of the form

$$p(x,t) = p_0(t) + M^2 \pi(x,t)$$

Thus, the pressure is decomposed into a thermodynamic component, p_0, that depends only on time and a perturbation component, π, that is $O(M^2)$. For the low Mach number model, we ignore the $O(M^2)$ effects on the thermodynamics. For simplicity, in this paper we will assume that the flow occurs in an open environment under constant pressure so that the thermodynamic pressure is, in fact, a constant which we denote as p_0. This leads to a modified momentum equation

$$\frac{\partial \rho U}{\partial t} + \nabla \cdot \rho U U = -\nabla \pi + \nabla \tau + \rho \mathbf{g}. \tag{1}$$

and reduces the enthalpy equation to

$$\frac{\partial \rho h}{\partial t} + \nabla \cdot (\rho U h) = \nabla \cdot \kappa \nabla T + \nabla \cdot \rho \xi_k D_k \nabla Y_k \tag{2}$$

The enthalpy and momentum equations combined with the species equations (and conservation of mass) describe the evolution of the low Mach number system. However, this evolution is also constrained by the equation of state. This constraint is equivalent to a constraint on the divergence of the velocity field that is obtained by differentiating the equation of state along particle paths

$$0 \equiv \frac{Dp}{Dt} = \frac{\partial p}{\partial \rho} \frac{D\rho}{Dt} + \frac{\partial p}{\partial T} \frac{DT}{Dt} + \frac{\partial p}{\partial Y_k} \frac{DY_k}{Dt} \quad .$$

Combining this equation with the mass conservation equation, we obtain

$$\nabla \cdot U = \frac{1}{\rho \frac{\partial p}{\partial \rho}} \left(\frac{\partial p}{\partial T} \frac{DT}{Dt} + \sum_k \frac{\partial p}{\partial Y_k} \frac{DY_k}{Dt} \right)$$

To complete the specification of the low Mach number model, we need to derive the temperature evolution equation. For this derivation, we express the enthalpy as a function of p, T, and Y_k. and differentiate the enthalpy equation to obtain

$$\frac{Dh}{Dt} = \left. \frac{\partial h}{\partial T} \right|_{p,Y_k} \frac{DT}{Dt} + \left. \frac{\partial h}{\partial p} \right|_{T,Y_k} \frac{Dp}{Dt} + \left. \frac{\partial h}{\partial Y_k} \right|_{p,T,Y_{j,j\neq k}} \frac{DY_k}{Dt}$$

After substituting from the above equations and using the low Mach number condition on p we have

$$\rho c_p \frac{DT}{Dt} = \nabla \cdot \kappa \nabla T + \rho D_k \nabla \xi_k \cdot \nabla Y_k - \rho \xi_k \dot{\omega}_k \qquad (3)$$

where $c_p = \left.\frac{\partial h}{\partial T}\right|_{p,Y_k}$ is the specific heat at constant pressure.

Substituting into the above equation for $\nabla \cdot U$ yields an expression for a constraint on the advective flow velocities:

$$\begin{aligned}
\nabla \cdot U &= \frac{1}{\rho \frac{\partial p}{\partial \rho}} \left(\frac{1}{\rho c_p} \frac{\partial p}{\partial T} (\nabla \cdot \kappa \nabla T + \rho D_k \nabla \xi_k \cdot \nabla Y_k - \rho \xi_k \dot{\omega}_k) \right. \\
&\quad + \left. \frac{1}{\rho} \frac{\partial p}{\partial Y_k} (\nabla \rho D_k \nabla Y_k + \rho \dot{\omega}_k) \right) \\
&\equiv S.
\end{aligned} \qquad (4)$$

3 Numerical methodology

In this section we discuss the numerical methodology used to integrate the low Mach number equations. The spatial discretization uses finite volume differencing with ρ, h, U, $\nabla \pi$ and the Y_k's defined on cell centers. The perturbational pressure is staggered in both space and time . Advection is discretized using a second-order Godunov-type procedure while diffusion is approximated with standard finite different methods. Our temporal discretization strategy is a fractional step approach based on a projection approximation. In this approach we integrate the equations for momentum, species and enthalpy using a lagged approximation to the constraint. We then apply a discrete projection to the intermediate velocity computed in the first step to enforce the constraint. This basic fractional step algorithm is embedded in a hierarchical adaptive mesh refinement (AMR) algorithm. The methodology presented here is documented in more detail in Day and Bell [15] for gaseous combustion and the extension to general equation of state is discussed in Bell *et al.* [5]. In the next subsection we describe the single-grid algorithm. We then discuss incorporation of that algorithm into an adaptive projection framework.

3.1 Single grid algorithm

The single grid algorithm is essentially a three-step process. First, we use an unsplit second-order Godunov procedure to predict a time-centered $(t^{n+1/2})$ advection velocity, $U^{\mathrm{ADV},*}$, using the cell-centered data at t^n and the lagged pressure gradient at $t^{n-1/2}$. The provisional field, $U^{\mathrm{ADV},*}$, represents a normal velocity on cell edges analogous to a MAC-type staggered grid discretization of the Navier-Stokes equations (see [18], for example). However, $U^{\mathrm{ADV},*}$ fails to

satisfy the time-centered divergence constraint. We apply a discrete projection by solving the elliptic equation

$$D^{\mathrm{MAC}} \frac{1}{\rho^n} G^{\mathrm{MAC}} \phi^{\mathrm{MAC}} = D^{\mathrm{MAC}} U^{\mathrm{ADV},*} - \left(S^n + \frac{\Delta t^n}{2} \frac{S^n - S^{n-1}}{\Delta t^{n-1}} \right) \qquad (5)$$

for ϕ^{MAC}, where D^{MAC} represents a centered approximation to a cell-based divergence from edge-based velocities, and G^{MAC} represents a centered approximation to edge-based gradients from cell-centered data. The solution, ϕ^{MAC}, is then used to define

$$U^{\mathrm{ADV}} = U^{\mathrm{ADV},*} - \frac{1}{\rho^n} G^{\mathrm{MAC}} \phi^{\mathrm{MAC}}.$$

U^{ADV} is a second-order accurate, staggered-grid vector field at $t^{n+\frac{1}{2}}$ that discretely satisfies the constraint (4), and is used for computing the advective derivatives for U, ρh and ρY_k.

In the next step of the algorithm we advance the advection-reaction-diffusion system for ρh and ρY_k. For the types of problems considered here, the reactions typically occur on a scale faster than the fluid dynamics. For that reason, we treat the reactions using a symmetric Strang-splitting approach so that the reactions can be treated with stiff ODE methodology. We first advance the reactions terms $\Delta t/2$ in time. We then advance the advection-diffusion part of the equation Δt in time followed by a second advancement of the reaction terms $\Delta t/2$ in time.

The reaction part of the enthalpy and species equations are of the form

$$\frac{\partial Y_k}{\partial t} = \dot{\omega}_k$$

and

$$c_p \frac{\partial T}{\partial t} = -\sum_k \xi_k \dot{\omega}_k$$

Here, we include the evolution of temperature as part of the system of ODE's integrated in the reaction step. We note, however, that for the reaction phase of the computation the enthalpy remains constant. Thus, the evolution of temperature can also be computed from the evolution of species by solving for the temperature given the updated composition and the (constant) enthalpy. We have not used this later approach because of the added computational expense; however, to preserve the conservation of energy we do not use the updated temperature from the reaction step to update the enthalpy. Instead, after the ODE integration, we recompute temperature from the enthalpy and final species concentrations.

In our implementation, we integrate the chemistry component using time-implicit backward difference methods, as implemented in VODE [12], a general-purpose stiff ODE integration software package. VODE utilizes adaptivity in

order of accuracy and subcycled time-step selection so that an absolute error tolerance of 10^{-16} in mass fractions is maintained throughout. Typically, the resulting scheme is between third and fifth order convergent in time.

After completing the first reaction step, we update the advection-diffusion component of the system. One numerical issue that must be addressed at this point is the nonlinearity of the enthalpy diffusion. To facilitate the solution of the enthalpy equation we rewrite the heat flux in terms of enthalpy diffusion

$$\frac{\partial \rho h}{\partial t} + \nabla \cdot U \rho h = \nabla \cdot \frac{\kappa}{c_p} \nabla h - \nabla \cdot \left(\sum_k \xi_k \frac{\kappa}{c_p} \nabla Y_k \right) + \nabla \cdot \rho D_k \xi_k \nabla Y_k \quad (6)$$

We advance the species equations and this modfied form of the enthalpy equations using a Crank-Nicolson treatment of diffusion and an explicit treatment of advection. For the diffusive terms, the coefficients D_k, ξ_k, κ and c_p are nonlinear functions of ρ, h and the Y_k's. We treat this nonlinearity using lagged coefficients in a simple iterative scheme. Two steps of this iteration are sufficient to guarantee second-order convergence of the scheme. Another issue in the treatment of these equations is that mixture models for species diffusion do not necessarily determine diffusion fluxes that sum to zero. A standard method for correcting this discrepancy is to define a "conservation diffusion velocity" as recommended by Coffee and Heimerl [14], and rigorously justified as a first term in a convergent series expression for full matrix diffusion by Giovangigli [17]. In the algorithm, we compute species diffusion implicitly then explictly apply this correction. The corrected diffusion fluxes will be denoted with an overbar.

We begin with data obtained by advancing the first half of the chemistry integration which we denote with a superscript n. We compute edge-centered states for ρY_k and T at $t^{n+\frac{1}{2}}$ using a second-order Godunov procedure. Time-centered edge values of ρY_k and T are used to compute $t^{n+\frac{1}{2}}$ edge values for $\rho = \sum \rho Y_k$ and ρh. We now update ρ using the discrete form of the continuity equation

$$\rho^{n+1} = \rho^n - \Delta t \; \nabla \cdot \left(\sum_k U^{ADV} \rho Y_k^{n+\frac{1}{2}} \right).$$

Given the updated density, we define $Y_k^{n+1,0} = Y_k^n$, $h^{n+1,0} = h^n$ and $T^{n+1,0} = T^n$ to initialize the nonlinear iteration of the diffusion coefficients.

With the current iterate we now compute the approximations to the terms required to form the diffusion coefficients, D_k, ξ_k, κ and c_p which we denote with the superscript $n+1, m$. We then solve for a provisional update to the mass fractions

$$\frac{\rho^{n+1}\tilde{Y}_k^{n+1,m} - \rho Y_k}{\Delta t} + \left(\nabla \cdot U^{ADV} \rho Y_k \right)^{n+\frac{1}{2}} = \quad (7)$$
$$\frac{1}{2} \nabla \cdot \left(\rho^{n+1} D_k^{n+1,m} \nabla \tilde{Y}_k^{n+1,m} + \overline{\rho^n D_k^n \nabla Y_k^n} \right).$$

After the solution of (7) the initial new-time fluxes, $-\rho^{n+1}D_k^{n+1,m}\nabla\tilde{Y}_k^{n+1,m}$ do not sum to zero. We again modify the fluxes using the correction velocity approach and use the result to correct the provisional update to the mass fractions

$$
\frac{\rho^{n+1}Y_k^{n+1,m} - \rho^n Y_k^n}{\Delta t} + \left(\nabla\cdot U^{ADV}\rho Y_m\right)^{n+\frac{1}{2}} =
$$
$$
\frac{1}{2}\left(\overline{\rho^{n+1}D_k^{n+1,m}\nabla\tilde{Y}_k^{n+1,m}} + \overline{\rho^n D_k^n \nabla Y_k^n}\right).
$$

We now update the enthalpy equation using

$$
\frac{\rho^{n+1}h^{n+1,m} - \rho^n h^n}{\Delta t} + \left(\nabla\cdot U^{ADV}\rho h\right)^{n+\frac{1}{2}} = \tag{8}
$$
$$
\frac{1}{2}\left[\nabla\cdot\frac{\kappa^{n+1,m}}{c_p^{n+1,m}}\nabla h^{n+1,m} + \nabla\cdot\frac{\kappa^n}{c_p^n}\nabla h^n\right]
$$
$$
+\frac{1}{2}\nabla\cdot\left[\xi_k^{n+1,m}\left(\overline{\rho^{n+1}D_k^{n+1,m}\nabla\tilde{Y}_k^{n+1,m}} - \frac{\kappa^{n+1,m}}{c_p^{n+1,m}}\nabla Y_k^{n+1,m}\right)\right.
$$
$$
\left. +\xi_k^n\left(\overline{\rho^n D_k^n \nabla Y_k^n} - \frac{\kappa^n}{c_p^n}\nabla Y_k^n\right)\right].
$$

Finally, we solve for an updated temperature, $T^{n+1,m}$, consistent with the new approximation to species and enthalpy. We note that two passes through this iteration is sufficient to guarantee second-order accuracy of the advection-diffusion component of the algorithm.

The integration of the enthalpy and species equations is completed by advancing the reaction part of the system an additonal $\Delta t/2$ in time. This provides a complete update of the ρ, h, T, and Y_k's at the new time and allows us to evaluate the constraint on the velocity field, S^{n+1}, at the new time.

The final step of basic integration step is to advance the velocity to the new time level. For this step we first obtain a provisional cell-centered velocity at t^{n+1} using a time-lagged pressure gradient,

$$
\rho^{n+\frac{1}{2}}\frac{U^{n+1,*} - U^n}{\Delta t} + \rho^{n+\frac{1}{2}}\left[(U^{ADV}\cdot\nabla)U\right]^{n+\frac{1}{2}} = \frac{1}{2}(\nabla\cdot\tau^* + \nabla\cdot\tau^n)
$$
$$
-\nabla\pi^{n-\frac{1}{2}} + \rho^{n+\frac{1}{2}}\mathbf{g}.
$$

At this point $U^{n+1,*}$ does not satisfy the constraint. We apply an approximate projection to simultaneously update the pressure and to project $U^{n+1,*}$ onto the constraint surface. In particular, we solve

$$
L^\rho\phi = D(U^{n+1,*} + \frac{\Delta t}{\rho^{n+\frac{1}{2}}}G\pi^{n-\frac{1}{2}}) - S^{n+1} \tag{9}
$$

for nodal values of ϕ, where L^ρ is the standard bilinear finite element approximation to $\nabla\cdot\frac{1}{\rho}\nabla$ with ρ evaluated at $t^{n+\frac{1}{2}}$. In this step, D is a discrete

second-order operator that approximates the divergence at nodes from cell-centered data, and $G = -D^T$ approximates a cell-centered gradient from nodal data. In the formulation, ϕ satisfies Neumann boundary conditions at solid walls and inflow boundaries. At outflow boundaries, Dirichlet conditions are generated to suppress any tangential accelerations on the fluid leaving the domain. Nodal values for S^{n+1} for the solution of (9) are computed using a volume-weighted average of cell-centered values. Finally, we determine the new-time cell-centered velocity field from

$$U^{n+1} = U^{n+1,*} - \frac{\Delta t}{\rho^{n+\frac{1}{2}}} \left(G\phi - G\pi^{n-\frac{1}{2}} \right)$$

and the new time-centered pressure from

$$\pi^{n+\frac{1}{2}} = \phi.$$

This completes the description of the time-advancement algorithm.

Before discussing the incorporation of this methodology in an adaptive mesh refinement algorithm, we note some of the properties of the algorithm. As noted earlier, although the scheme rigorously satisfies conservation of mass and enthalpy, the evolution does not strictly maintain the equation of state at ambient pressure. (It is not possible to preserve all three conditions in a projection-type fractional step scheme.) Since the low Mach number asymptotics used to derive the governing equation show that the thermodynamic pressure only satisfies this constraint to $O(M^2)$, relaxing the imposition of the constraint is a reasonable way of dealing with splitting errors. To control the deviation from the equation of state we add a correction to the right hand side of equation (5) that approximates

$$\frac{f}{\gamma \rho \frac{\partial p}{\partial \rho}} \left(\frac{\partial p}{\partial t} + U \cdot \nabla p \right).$$

In this expression $\gamma = c_p/c_v$ is the ratio of the two thermodynamic specific heats, and f is a constant relaxation factor. We approximate $\partial p/\partial t$ by $(p_{\text{amb}} - p_0)/\Delta t$, where p_0 is the thermodynamic pressure defined by ρ, h and the Y_k's and p_{amb} is the specified ambient pressure, and $U \cdot \nabla p$ is approximated with upwind differences using p_0. Thus, we are effectively adding a first-order approximation to the material derivative of $p_0 - p_{\text{amb}}$ along streamlines. This forcing term adjusts the advection velocity to drive the evolution toward the constraint, preventing the solution from deviating an appreciable amount from the equation of state while maintaining the second-order accuracy of the overall scheme.

3.2 Adaptive mesh refinement

In this section we present an overview of the adaptive projection algorithm. This framework, used in both Day and Bell [15] and Bell *et al.* [5] was initially

developed by Almgren *et al.* [1], and extended to low Mach number combustion by Pember *et al.* [28]. The discussion provides only an overview of the methodology. We refer the reader to the above papers for more details of the basic algorithm.

Our implementation of adaptive mesh refinement (AMR) is based on a sequence of nested grids with successively finer spacing in both time and space. In this approach, fine grids are formed by evenly dividing coarse cells by a refinement ratio, r, in each direction. Increasingly finer grids are recursively embedded in coarse grids until features of the solution are adequately resolved. An error estimation procedure based on user-specified criteria evaluates where additional refinement is needed and grid generation procedures dynamically create or remove rectangular fine grid patches as resolution requirements change.

The adaptive integration algorithm advances grids at different levels using time steps appropriate to that level, based on CFL considerations. The multi-level procedure can most easily be thought of as a recursive algorithm in which, to advance level ℓ, $0 \leq \ell \leq \ell_{\max}$, the following steps are taken:

- Advance level ℓ in time one time step, Δt^ℓ, as if it is the only level. If $\ell > 0$, obtain boundary data using time-interpolated data from the grids at $\ell - 1$, as well as physical boundary conditions, where appropriate.
- If $\ell < \ell_{\max}$
    - Advance level $(\ell+1)$ for r time steps, $\Delta t^{\ell+1} = \frac{1}{r}\Delta t^\ell$, using level-$\ell$ data and the physical boundary conditions.
    - Synchronize the data between levels ℓ and $\ell + 1$, and interpolate corrections to finer levels $[\ell + 2, \dots, \ell_{\max}]$.

The adaptive algorithm, as outlined above, performs operations to advance the grids at each level independent of other levels in the hierarchy (except for boundary conditions) and then computes a correction to synchronize the levels. Loosely speaking, the objective in this synchronization step is to compute the modifications to the coarse grid that reflect the change in the coarse grid solution due to the presence of the fine grid. More specifically, when solving on a fine grid, we supply Dirichlet boundary conditions from the coarse grid. This leads to a mismatch in the associated fluxes at the coarse-fine interface that is corrected by the synchronization.

For the adaptive projection methodology presented here there are three basic steps in the synchronization. First, the values obtained for U, ρY_k and ρh are averaged from the fine grid onto the underlying coarse grid. We view the resulting data as defining a preliminary composite grid solution that is consistent between levels. We denote this preliminary solution with a p superscript in the remainder of the section. To complete the synchronization we need to correct inconsistencies arising from the use of Dirichlet boundary conditions at coarse-fine boundaries. In particular, we compute increments to ρY_k and ρh that correct the flux mismatches at coarse-fine interfaces. Finally, we

correct the velocity field to satisfy a divergence constraint on the composite grid system.

There are two components that contribute to flux mismatch. First, U^{ADV}, the edge-based advection velocity satisfies the constraint on the coarse level and the fine level separately. However, since we only satisfy the Dirichlet matching condition for ϕ^{MAC} in (5), the value of U^{ADV} computed on the coarse level does not match the average value on the fine grid. We define the mismatch in advection velocities in d dimensions by

$$\delta U^{\mathrm{ADV},\ell} = -U^{\mathrm{ADV},\ell,n+\frac{1}{2}} + \frac{1}{r^d}\sum_{k=0}^{r-1}\sum_{\mathrm{edges}} U^{\mathrm{ADV},\ell+1,n+k+\frac{1}{2}}$$

along the coarse-fine boundary. We then solve the elliptic equation

$$D^{\mathrm{MAC}}\frac{1}{\rho}G^{\mathrm{MAC}}\delta e^\ell = D^{\mathrm{MAC}}\delta U^{\mathrm{ADV},\ell}$$

and compute

$$U^{\mathrm{ADV},\ell,\mathrm{corr}} = -\frac{1}{\rho}G^{\mathrm{MAC}}\delta e^\ell$$

which is the correction needed for U^{ADV} to satisfy the constraint and matching conditions on the composite $(\ell,\ \ell+1)$ grid hierarchy. This correction field is used to compute a modification to the advective fluxes for species and enthalpy that reflects an advection velocity field that satisfies the constraint on the composite grid.

The second part of the mismatch arises because the advective and diffusive fluxes on the coarse grid were computed without explicitly accounting for the fine grid, while on the fine grid the fluxes were computed using coarse-grid Dirichlet boundary data. We define the flux discrepancies

$$\delta F_{\rho h} = \Delta t^\ell \left(-F_{\rho h}^{\ell,n+\frac{1}{2}} + \frac{1}{r^d}\sum_{k=0}^{r-1}\sum_{edges} F_{\rho h}^{\ell+1,n+k+\frac{1}{2}} \right)$$

and

$$\delta F_{\rho Y_k} = \Delta t^\ell \left(-F_{\rho Y_k}^{\ell,n+\frac{1}{2}} + \frac{1}{r^d}\sum_{k=0}^{r-1}\sum_{edges} F_{\rho Y_k}^{\ell+1,n+k+\frac{1}{2}} \right)$$

where F is the total (advective+diffusive) flux through a given interface prior to these synchronization operations. Corrections to density, $\delta\rho^{sync}$, on the coarse grid associated with mismatched advection fluxes may be computed explicitly

$$\delta\rho^{sync} = -D^{MAC}\left(\sum_k U^{ADV,corr}\rho Y_k\right)^{n+\frac{1}{2}} + \sum_k \delta F_{\rho Y_k}.$$

The post-sync new-time value of density is given by $\rho^{n+1} = \rho^{n+1,p} + \delta\rho^{sync}$. Given the corrected density, ρ^{n+1}, we can decompose the corrections for Y_k and h into

$$\delta\left(\rho Y_k\right)^{sync} = Y_k^{n+1,p}\delta\rho^{sync} + \rho^{n+1}\delta Y_k^{sync}$$

and

$$\delta\left(\rho h\right)^{sync} = h^{n+1,p}\delta\rho^{sync} + \rho^{n+1}\delta h^{sync}.$$

Computing δY_k^{sync} and δh^{sync} requires solution of a linear system, since the flux mismatch contains implicit diffusion fluxes from the Crank-Nicolson discretization. The provisional correction $\delta\tilde{Y}_k^{sync}$ on the coarse level ℓ grids is obtained by solving

$$\left(\rho^{n+1} - \frac{\Delta t}{2}\nabla\rho^{n+1}D_k^{n+1}\nabla\right)\delta\tilde{Y}_k^{sync} = -D^{MAC}\left(U^{ADV,corr}\rho Y_k\right)^{n+\frac{1}{2}} + \delta F_{\rho Y_k}.$$

However, as in the single-level algorithm, the species correction fluxes must sum to zero to preserve mass conservation. We compute the adjusted species diffusion correction fluxes which sum to zero and then define Y_k^{sync} from

$$\rho^{n+1}\delta Y_k^{sync} = \frac{\Delta t}{2}\nabla\overline{\rho^{n+1}D_k^{n+1}\nabla\delta\tilde{Y}_k^{sync}} - D^{MAC}\left(U^{ADV,corr}\rho Y_k\right)^{n+\frac{1}{2}} + \delta F_{\rho Y_k}.$$

We then compute the enthalpy correction from

$$\left(\rho^{n+1} - \frac{\Delta t}{2}\nabla\rho^{n+1}\frac{\kappa^{n+1}}{c_p^{n+1}}\nabla\right)\delta h^{sync} = -D^{MAC}\left(U^{ADV,corr}\rho h\right)^{n+\frac{1}{2}} + \delta F_{\rho h}$$

$$+\nabla\cdot\xi_k\left(\frac{\kappa^{n+1}}{c_p^{n+1}}\nabla\delta Y_k^{sync} - \overline{\rho^{n+1}D_k^{n+1}\nabla\delta\tilde{Y}_k^{sync}}\right).$$

The corrections, δY_k^{sync}, and δh^{sync} are added to the coarse field at level ℓ, and interpolated to all finer levels. Finally, a new temperature field is computed using the corrected h and Y_k's.

A similar process is also used to generate a correction to the velocity field. However, the velocity flux correction must be projected to obtain the component satisfying the constraint that updates U and the component that updates π. At this point there are two additional corrections needed for the composite velocity field:

- A correction arising because the projection at level $\ell + 1$ used Dirichlet data from level ℓ, leading to a mismatch in normal derivative at coarse-fine boundaries
- The temperature and species adjustment in the first part of the synchronization leads to an increment in the computed S field.

Since the projection is linear, both of these corrections as well as the projection of the velocity flux correction can be combined into a single, multi-level node-based synchronization solve performed at the end of a coarse-grid time step.

We note that with the synchronization procedure outlined above the adaptive algorithm preserves the second-order accuracy and the conservation properties of the single-grid algorithm. The methodology has been implemented for distributed memory parallel processors using the BoxLib class libraries described by Rendleman et al. [30]. Futher discussion of the parallelization of the low Mach number model can be found in Bell *et al.* [4].

4 Combustion

In this section, we present a prototype application of the above methodology to turbulent combustion. The results presented here are taken from a study by Bell *et al.* [7]. The goal of this study was to assess the resolution requirements needed to capture the dominant features of an experimental methane flame using detailed chemistry and transport without explict models for turbulence or turbulence chemistry interaction. A photograph of the experiment is present in Figure 1. In the experiment, a plate with 3.2 mm holes arranged in a 4.8 mm hexagonal lattice is placed in the inflow stream 9 cm below the exit to the nozzle. A 2 mm rod is placed across the nozzle exit where it serves to anchor a turbulent V-flame.

The computational strategy for this simulation is to independently characterize the turbulence generation in the nozzle using experimental data and auxiliary computations. Turbulent fluctuations with appropriate statistical properties are then superimposed on the mean inflow velocity. For the case considered here the inflow velocity is 3 m/sec with a turbulent intensity of approximately 7% in the axial direction and 5% in the transverse directions. The inflow conditions correspond to methane at an equivalence ratio of 0.75 at 300K.

With this characterization of the inflow we solve the low Mach number equations in a cubical domain indicated in Figure 1. For this computation, methane chemistry was modeled using the methane mechanism, DRM-19, developed by Frenklach which contains 19 species and 84 reactions. A mixture model was used for species diffusion. The computation was performed with a base grid of 96^3 with 2 refinements of a factor of 2 each. This lead to an effective resolution of approximately 312.5 μm which corresponds to approximately 2-3 zones across the thermal thickness of the flame.

A picture of the computed flame surface is presented in Figure 2. Figure 3 presents a quantitative comparison of the computed solution to the experimental data. Experimentally, the instantaneous flame location is determined from PIV measurements. Due to the large difference in Mie scattering intensities from the reactants and products, the instantaneous wrinkled flame front is clearly outlined on the PIV image (Figure 3b). Compared to a centerline slice of the methane concentration obtained from the simulation (Figure 3a) the wrinkling of the flame in the experiment and the computation is similar in size and structure.

To characterize the flame brush which gives a statistical picture of the flame, the position of the flame fronts were obtained from 100 PIV images by an edge detection algorithm. Their average produces a map of the mean reaction progress, $\bar{c}$, where $\bar{c} = 0$ in reactants, and $\bar{c} = 1$ in the products. For the simulation data, we define an instantaneous progress variable $c = (\rho_u - \rho)/(\rho_u - \rho_b)$ where $\rho_{u,b}$ are the densities of the unburned and burned gas, respectively. Averaging c over a sample of slices through the computed flame defines an analogous $\bar{c}$ for the computation.

A comparison of experimental and computational $\bar{c}$ contours which show the growth of the flame brush is given in Figure 4. The simulation shows excellent agreement up to approximately $z < 10$ cm at which point the computational results begin to show the effects of the outflow imposed at $z = 12$ cm. The simulation and the experimental results have slightly different included angles; the $\bar{c} = 0.5$ contour forms an angle of approximately $11°$ with the vertical in the experiment compared to $13°$ for the computation. Additional comparisons with the experimental data are presented in Bell *et al.* [7].

5 Nuclear flames

In the second example, we consider $C + O$ nuclear flames in a carbon-oxygen white dwarf typical of a Type Ia supernova. The results presented here are taken from a study of the effect of Rayleigh-Taylor instabilites on flame propagation at conditions corresponding to the late stages of a type Ia supernova by Bell *et al.* [6]. For this example a generalized equation of state is needed to describe the fluid. In particular, for the stellar conditions being considered here the pressure contains contributions from ions, radiation, and electrons. (See Kippenhahn and Weigert [20] for a discussion of equations of state for stellar matter.) Thus,

$$p = p_{\text{ion}} + p_{\text{rad}} + p_{\text{ele}} \tag{10}$$

with

$$p_{\text{ion}} = \frac{\rho k T}{\bar{A} m_p} \quad , \quad p_{\text{rad}} = aT^4/3$$

and p_{ele} is the contribution to the thermodynamic pressure due to fermions. In these expressions, m_p is the mass of the proton, a is related to the Stefan-Boltzmann constant $\sigma = ac/4$, c is the speed of light, $1/\bar{A} = X_k/A_k$, and k is Boltzmann's constant. The ionic component has the form associated with an ideal gas but the radiation and electron pressure components do not. The numerical simulations were performed using the equation of state described by Timmes and Swesty [33] which computes the internal energy, pressure and thermodynamic derivatives (including the specific heats at constant volume and pressure) of these quantities as functions of temperature, density and the nuclear-species mass fractions.

For the stellar conditions typical of C + O flames we are considering here, the Lewis number, which is the ratio of energy transport to species diffusion,

is $O(10^7)$ and the Prandtl number, which is the ratio of fluid viscosity to energy transport, is $O(10^{-5})$. For these conditions, we can ignore both fluid viscosity and species diffusion. The values of the thermal conductivity, κ, are calculated using the procedure described by Timmes [32].

We present computations corresponding to fuel densities of 1.5×10^7 g/cc and 1.0×10^7 g/cc. For each simulation, $g = 10^9$cm/sec^2 which is appropriate for the outer region of the white dwarf after some pre-expansion has taken place. We flow fuel in from the top of the domain at the laminar flame velocity and impose an outflow boundary condition at the bottom of the domain. The lateral sides of the domain are periodic. Each computation is performed with one level of refinement with an effective resolution that is approximately 10% of the thermal flame thickness. The domains are 163.84 cm ×327.7 cm and 53.5 cm ×107 cm for the low and high density cases, respectively, which correspond to approximately 90 thermal flame thicknesses in each case.

Figures 5 and 6 correspond to the high and low density cases, respectively. This range of densities represents a transition from flamelet combustion at the higher density in which a clearly defined flame front is apparent to a distributed flame in which the reactions occur in dispersed pockets at the lower density. Analyses of these types of simulations are being used to help determine how much the flame is accelerated by interaction with the Rayleigh-Taylor instability which plays a key role in determining the mechanisms that lead to type Ia supernova explosions.

6 Conclusion

We have presented an adaptive algorithm for reacting flows based on a low Mach number formulation. This formulation, which leads to constrained evolution equations, analytically removes sound waves from the system and allows time steps to be chosen based on the advective time scales. The low Mach number system is integrated using a fractional step projection algorithm that evolves the system without enforcing the constraints and then projects the solution back onto the constraint manifold. The basic projection discretization has been incorporated into a parallel adaptive mesh refinement algorithm. We have shown two examples of problems that would have been infeasible without this type of methodology.

Acknowledgement

References

1. A. S. Almgren, J. B. Bell, P. Colella, L. H. Howell, and M. Welcome. A conservative adaptive projection method for the variable density incompressible Navier-Stokes equations. *J. Comput. Phys.*, 142:1–46, 1998.
2. A. S. Almgren, J. B. Bell, P. Colella, L. H. Howell, and M. L. Welcome. A conservative adaptive projection method for the variable density incompressible Navier-Stokes equations. 142:1–46, May 1998.
3. R. Becker, M. Braack, and R. Rannacher. Numerical simulation of laminar flames at low mach number by adaptive finite elements. *Combust. Theory Modelling*, 3:503–534, 1999.
4. J. B. Bell, M. S. Day, A. S. Almgren, M. J. Lijewski, and C. A. Rendleman. A parallel adaptive projection method for low Mach number flows. *Int. J. Numer. Meth. Fluids*, 40:209–216, 2002.
5. J. B. Bell, M. S. Day, C. A. Rendleman, S. E. Woosley, and M. A. Zingale. Adaptive low mach number simulations of nuclear flames. Technical Report LBNL-52395, Lawrence Berkeley National Laboratory, March 2003. to appear in J. Comp. Phys.
6. J. B. Bell, M. S. Day, C. A. Rendleman, S. E. Woosley, and M. A. Zingale. Direct numerical simulations of type ia supernovae flames ii: The rayleigh-taylor instability. Technical Report LBNL-54300, Lawrence Berkeley National Laboratory, January 2004. submitted Astrophysical Journal.
7. J. B. Bell, M. S. Day, I. G. Shepherd, M. Johnson, R. K. Cheng, V. E. Beckner, M. J. Lijewski, and J. F. Grcar. Numerical simulation of a laboratory-scale turbulent v-flame. Technical Report LBNL-54198, Lawrence Berkeley National Labortory, 2003. submitted Proceedings of the Combustion Institute.
8. J. B. Bell and D. L. Marcus. A second-order projection method for variable density flows. 101(2):334–348, August 1992.
9. B. A. V. Bennett, C. S. McEnally, L. D. Pfefferle, and M. D. Smooke. Computational and experimental study of axisymmetric coflow partially premixed methane/air flames. *Combust. Flame*, 123:522–546, 2000.
10. B.A.V. Bennett and M. D. Smooke. Local rectangular refinement with application to axisymmetric laminar flames. *Combust. Theory Modelling*, 2:221–258, 1998.
11. R. B. Bird, W. E. Stewart, and E. N. Lightfoot. *Transport Phenomena*. Wiley, New York, 2 edition, 2002.
12. P. N. Brown, G. D. Byrne, and A. C. Hindmarsh. VODE: A variable coefficient ode solver. *SIAM J. Sci. Stat. Comput.*, 10:1038–1051, 1989.
13. P.J. Coelho and J.C.F. Pereira. Calculation of a confined axisymmetric laminar diffusion flame using a local grid refinement technique. *Combust. Sci. Tech.*, 92:243–264, 1993.
14. T. P. Coffee and J. M. Heimerl. Transport algorithms for premixed laminar steady-state flames. *Comb. Flame*, 43:273, 1981.
15. M. S. Day and J. B. Bell. Numerical simulation of laminar reacting flows with complex chemistry. *Combust. Theory Modelling*, 4:535–556, 2000.
16. H.C. de Lange and L.P.H. de Goey. Numerical modeling in a locally refined grid. *Int. Jour. Num. Mech. Eng.*, 37:497–515, 1994.
17. V. Giovangigli. Convergent iterative methods for multicomponent diffusion. *IMPACT Comput. Sci. Engrg.*, 3:244–276, 1991.

18. F. H. Harlow and J. E. Welch. Numerical calculation of time-dependent viscous incompressible flow of fluids with free surfaces. *Physics of Fluids*, 8:2182–2189, 1965.

19. J. Hilditch and P. Colella. A front tracking method for compressible flames in one dimension. *SIAM J. Sci. Comput.*, 16:755–772, 1995.

20. Rudolf Kippenhahn and Alfred Weigert. *Stellar Structure and Evolution.* Springer Verlag, 1992.

21. M. F. Lai. *A Projection Method for Reacting Flow in the Zero Mach Number Limit.* PhD thesis, University of California at Berkeley, 1993.

22. M. F. Lai, J. B. Bell, and P. Colella. A projection method for combustion in the zero Mach number limit. In *Proceedings of the Eleventh AIAA Computational Fluid Dynamics Conference*, pages 776–783, 1993.

23. A. Majda and J. A. Sethian. The derivation and numerical solution of the equations for zero Mach number combustion. *Combust. Sci. Tech.*, 42:185–205, 1985.

24. R.M.M. Mallens, H.C. de Lange, C.H.J. van de Ven, and L. P. H. de Goey. Modeling of confined and unconfined laminar premixed flames on slit and tube burners. *Combust. Sci. Tech.*, 107:387–401, 1995.

25. P.A. McMurtry, W.-H. Jou, J.J. Riley, and R.W. Metcalfe. Direct numerical simulations or a reacting mixing layer with chemical heat release. *AIAA J.*, 24:962, 1986.

26. H.N. Najm, R.W. Schefer, R.B. Milne, C.J. Mueller, K.D. Devine, and S.N. Kempka. Numerical and experimental investigation of vortical flow–flame interaction. Technical Report SAND98-8232, Sandia National Laboratory, February 1998.

27. R. B. Pember, A. S. Almgren, J. B. Bell, P. Colella, L. H. Howell, and M. Lai. A higher-order projection method for the simulation of unsteady turbulent nonpremixed combustion in an industrial burner. *Transport Phenomena in Combustion*, pages 1200–1211, 1996. Taylor and Francis.

28. R. B. Pember, L. H. Howell, J. B. Bell, P. Colella, W. Y. Crutchfield, W. A. Fiveland, and J. P. Jessee. An adaptive projection method for unsteady, low-Mach number combustion. *Comb. Sci. Tech.*, 140:123–168, 1998.

29. R.G. Rehm and H.R. Baum. The equations of motion for thermally driven buoyant flows. *N. B. S. J. Res.*, 83:297–308, 1978.

30. Charles A. Rendleman, Vincent E. Beckner, Mike Lijewski, William Y. Crutchfield, and John B. Bell. Parallelization of structured, hierarchical adaptive mesh refinement algorithms. *Computing and Visualization in Science*, 3(3):147–157, 2000.

31. L.T. Somers and L.P.H. de Goey. A numerical study of a premixed flame on a slit burner. *Combust. Sci. Tech.*, 108:121–132, 1995.

32. Frank X. Timmes. The physical properties of laminar helium deflagrations. *Astrophysical Journal*, 528:913, 2000.

33. Frank X. Timmes and F. Douglas Swesty. The accuracy, consistency, and speed of an electron-positron equation of state based on table interpolation of the helmholtz free energy. *Astrophysical Journal Supplement*, 126:501–516, 2000.

34. M. D. Smooke A. A. Turnbull, , R. E. Mitchell, and D. E. Keyes. Solution of two-dimensional axisymmetric laminar diffusion flames by adaptive boundary value methods. In *Mathematical Modeling in Combustion and Related Topics*, pages 261–300, 1988.
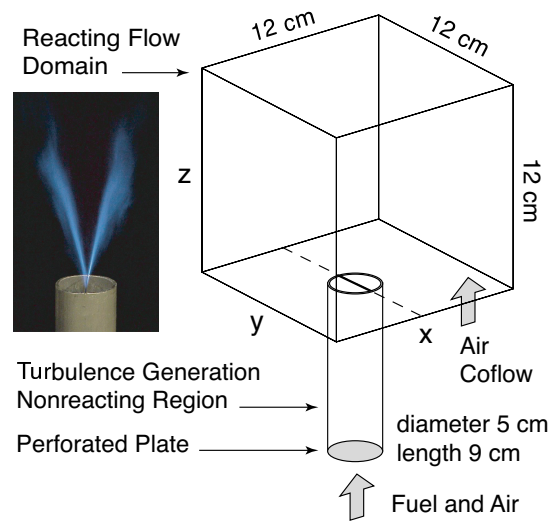
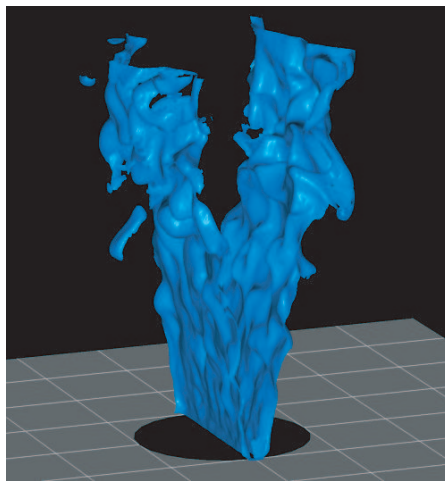**Fig. 1.** *Photograph of the experiment and schematic for the V-flame computation*

Fig. 2. *Simulated instantaneous flame surface*
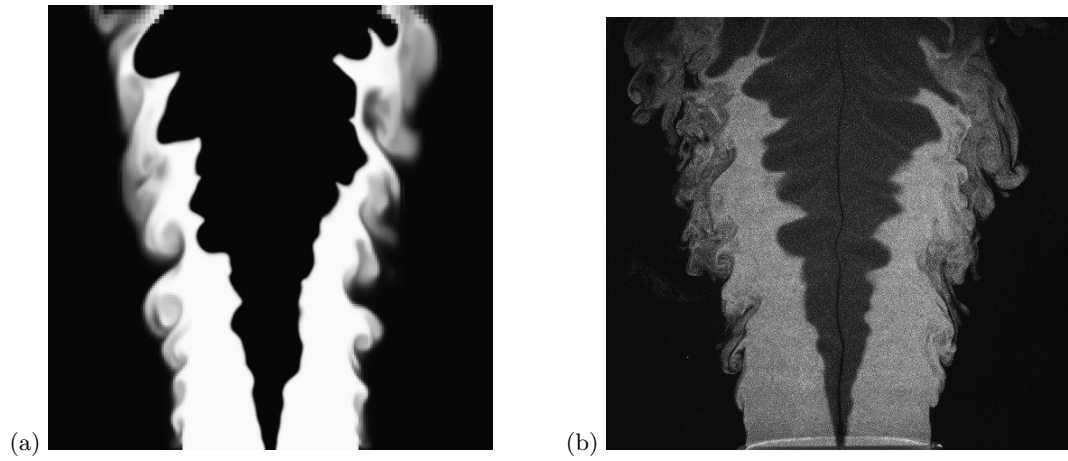
(a) (b)

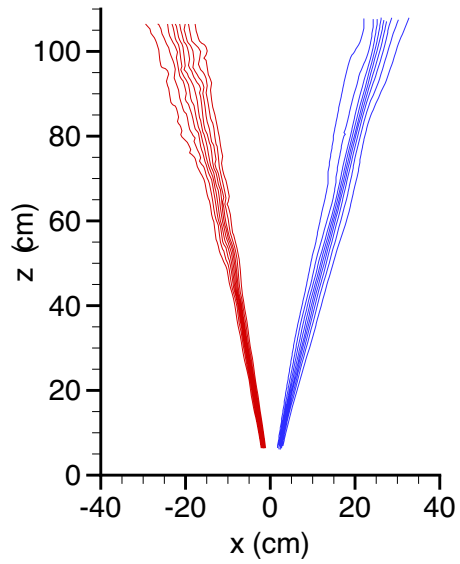**Fig. 3.** *(a) Computed CH_4 mole fraction, (b) Typical PIV image.*

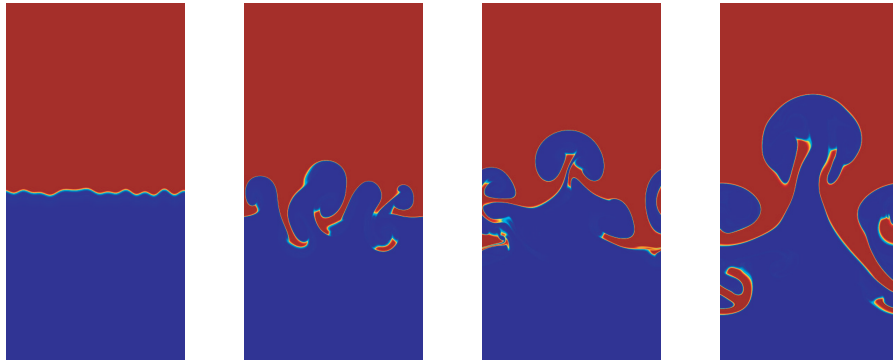**Fig. 4.** *Comparison of $\bar{c}$ contours. Left (red) is experiment; right (blue) is simulation*

Fig. 5. *Time sequence of Rayleigh Taylor unstable nuclear flame at density fuel density* 1.5×10^7 *g/cc. Times are 0.0, 0.7, 1.1 and 1.4 msec. The image shows carbon mass fraction with red to blue corresponding to high to low values.*
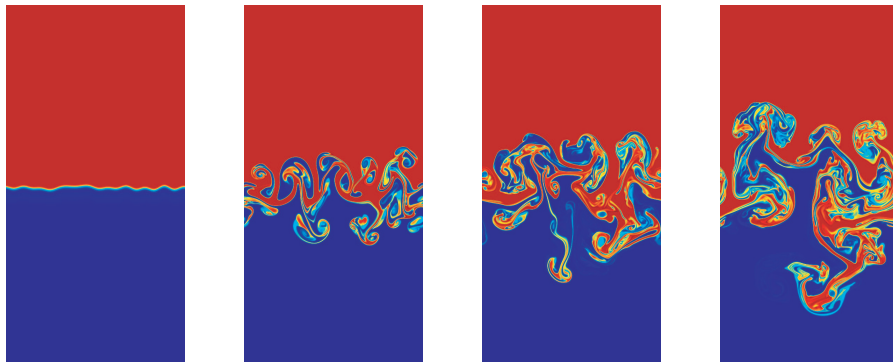

Fig. 6. *Time sequence of Rayleigh Taylor unstable nuclear flame at density fuel density* 1.0×10^7 *g/cc. Times are 0.0, 1.2, 1.8, and 2.3 msec. The image shows carbon mass fraction with red to blue corresponding to high to low values.*